# Multidomain Analytical–Numerical Solution for a Rotating Magnetic Field with a Finite-Length Conducting Cylinder

L. Martin Witkowski, P. Marty, and J. S. Walker

***Abstract*—This paper treats the rotating magnetic field produced by a cylindrical sheet of temporally and azimuthally periodic axial electric current with a finite-length, electrically conducting cylinder surrounded by an electrical insulator inside the current sheet. As the frequency is increased, the magnetic field produced by the induced current in the cylinder cancels progressively more of the current-sheet magnetic field in the interior of the cylinder. This paper presents results for several different frequencies and for several different length-to-diameter ratios for the cylinder. It compares the results at the midplane of a long cylinder to the analytical solution for an infinitely long cylinder. It also compares results for a high frequency to the predictions from the first two terms in an asymptotic expansion for high frequency.**

***Index Terms*—Bessel functions, cylinders, electromagnetic induction, finite difference methods, magnetohydrodynamics, partial differential equations.**

## I. Introduction

THIS PAPER presents numerical results for the periodic magnetic field produced in a conducting cylinder by a cylindrical sheet of axial electric current whose current density varies periodically with both time and the azimuthal coordinate. There is a finite-length, electrically conducting cylinder that lies along the centerline of the current sheet and whose radius is smaller than that of the current sheet. The rest of the interior of the current sheet is an electrical insulator. Such an azimuthally and temporally periodic magnetic field, often called a rotating magnetic field (RMF), has a constant spatial pattern which rotates at an angular velocity related to the frequency of the periodic electric current and the number of poles. There are many important applications of RMF's. For example, RMF's have been used for many years to stir molten steel or aluminum during the continuous casting of cylindrical billets [1], and recently RMF's have been used to stir the liquid during the growth of semiconductor crystals from a melt [2].

We focus on the geometry for crystal-growth applications in which the electrically conducting cylinder represents the liquid, and the electrical insulator represents the crystal, ampoule or crucible, atmosphere inside the crystal-growth furnace, etc. For most semiconductors, the liquid behaves as a liquid metal with a large electrical conductivity, while the solid has a much smaller electrical conductivity, e.g., a 20-to-1 ratio for silicon. To date, most models of crystal growth with RMF's have assumed that the frequency of the RMF is sufficiently low and that the magnetic field penetrates instantly across the entire liquid region because the magnetic field due to the induced electric current in the liquid is negligible [3]. However, RMF's with higher frequencies, such as 400 Hz, may have advantages over low-frequency RMF's, and for large systems, such as the Czochralski process, the induced magnetic field is not negligible for 50 Hz.

There are several major differences between induction heating and RMF's that preclude transfer of the induction-heating modeling methods to RMF problems [4]–[6]. For RMF's, all three components of the magnetic field are nonzero everywhere, and all three components of the electric current density are nonzero in the conductor. The azimuthal variation of the magnetic field and electric current preclude the use of the stream functions and Green's functions used for the axisymmetric variables in induction heating or levitation problems.

If both the conducting cylinder and the current sheet are infinitely long, then there is only a plane, two-dimensional problem governing $B_r(r, \theta)$, $B_\theta(r, \theta)$, and $j_z(r, \theta)$, where $r$, $\theta$, $z$ are cylindrical coordinates with the units vectors $\boldsymbol{e}_r$, $\boldsymbol{e}_\theta$, $\boldsymbol{e}_z$ and with the $z$ axis along the common centerline of the electrical conductor and of the concentric current sheet. Solutions for the magnetic field and for the stirring of the liquid were presented by Martin Witkowski and Marty [7] for any frequency. For the three-dimensional, nonaxisymmetric RMF with a finite-length conducting cylinder, there appears to be only one paper in the literature by Mazuruk *et al.* [8]. Their solution differs from the present one in several ways. They assume that the radius of the current sheet producing the RMF is infinite. Their solution involves two analytical solutions: one for the electrically insulating exterior of the cylinder and one for its electrically conducting interior. Matching the two analytical solutions at the exterior surfaces of the conductor leads to some extremely complex equations, the numerical solution of which required a simplification that limits the validity of the results to relatively low frequencies. Therefore, their solution represents a major advance over the common neglect of induced magnetic fields, but it is still limited to combinations of the frequency and cylinder radius for which the shielding parameter is less than a certain value.

Manuscript received February 23, 1999; revised August 31,1999. This work was supported by the U.S. National Aeronautics and Space Administration under Grant NAG 8-1453.

L. Martin Witkowski and J. S. Walker are with the Department of Mechanical and Industrial Engineering, University of Illinois, Urbana, IL 61801 USA (e-mail: witko@uiuc.edu; jswalker@uiuc.edu.).

P. Marty is with the Laboratoire des Ecoulements, Géophysiques et Industriels, IMG(CNRS-UJF-INPG) BP53X-38041 Grenoble Cedex, France (e-mail: Philippe.Marty@cea.fr).

Publisher Item Identifier S 0018-9464(00)01829-X.

In our solution, the radius of the current sheet is arbitrary, although we do assume that it is infinitely long. Our approach involves matching numerical solutions for the conducting cylinder and for the insulator in the annular region between cylinder and the current sheet with an analytical solution for the insulator in the semi-infinite cylindrical domain axially beyond either end of the cylinder. With the caveat that one must numerically resolve the skin-depth layers adjacent to the conductor's exterior surfaces for high frequencies, our model gives accurate results over the entire range from low frequencies to extremely high frequencies. Indeed, this model with appropriate spatial resolution gives better results for extremely high frequencies than those obtained from the first two terms in an asymptotic solution for large shielding parameter because the asymptotic solution introduces physically unrealistic discontinuities at the top and bottom circumferences of the conducting cylinder.

## II. Problem Formulation

We consider an electrically conducting cylinder that has a radius $R$ and an axial length $2hR$, which is surrounded by an electrical insulator, and which is subjected to a rotating magnetic field produced by a temporally and azimuthally periodic axial electric-current sheet at an infinitely long, concentric, cylindrical surface with a radius $aR$, where $a > 1$. For the current sheet, the electric current per unit length in the azimuthal direction is $\boldsymbol{J} = -J_o \cos(p\theta - \omega t)\boldsymbol{e}_z$, where $J_o$ is the peak current, $2p$ is the number of poles of the magnetic field, $\omega$ is the circular frequency, and $t$ is time. The geometry is sketched in Fig. 1 with $r$, $z$ and all lengths normalized by $R$. The material around the current sheet has an infinite magnetic permeability, while both the conducting cylinder and the insulator inside the current sheet have the magnetic permeability $\mu_0$ of a vacuum. For $r < a$, the electric field $\boldsymbol{E}$, the magnetic field $\boldsymbol{B}$, and the electric current density $\boldsymbol{j}$ are governed by Maxwell's equations neglecting displacement currents

$$\nabla \times \boldsymbol{E} = -\frac{\partial \boldsymbol{B}}{\partial t} \tag{1}$$

$$\nabla \times \left(\frac{\boldsymbol{B}}{\mu_0}\right) = \boldsymbol{j} \tag{2}$$

$$\nabla \cdot \boldsymbol{B} = 0 \tag{3}$$

$$\nabla \cdot \boldsymbol{j} = 0. \tag{4}$$

We also have $\boldsymbol{j} = 0$ for the insulator and Ohm's law

$$\boldsymbol{j} = \sigma \boldsymbol{E} \tag{5}$$

for the conductor, where $\sigma$ is its electrical conductivity. If the electrical conductor is a liquid, then Ohm's law (5) assumes that the liquid's velocity is much smaller than $\omega R$ [9].

The boundary condition on $\boldsymbol{B}$ at the current sheet is

$$B_\theta = \mu_0 J_o \cos(p\theta - \omega t), \qquad \text{at } r = a. \tag{6}$$

With (2) and (6), $B_z$ is automatically zero at $r = a$. All components of $\boldsymbol{B}$ are continuous across the boundaries at $r = 1$ and $z = \pm h$ between the conductor and the insulator. In the conductor

$$j_r = 0, \qquad \text{at } r = 1 \tag{7}$$

$$j_z = 0, \qquad \text{at } z = \pm h. \tag{8}$$

Because of the symmetry, we need only treat $0 \le z < \infty$ with suitable symmetry conditions at $z = 0$. Neglecting the transient when the current sheet starts, $\boldsymbol{B}$, $\boldsymbol{j}$, and $\boldsymbol{E}$ have the form

$$\boldsymbol{B} = \Re e\left[\boldsymbol{B}^*(r, z)e^{i(p\theta - \omega t)}\right] \tag{9}$$

where $\boldsymbol{B}^* = \Re e(\boldsymbol{B}^*) + i\Im m(\boldsymbol{B}^*)$ is the complex modal function. Henceforth all variables are complex modal functions of $r$ and $z$, so that we drop the asterisks.

In the insulator $\boldsymbol{j} = 0$, so that we can introduce a complex potential function $\psi(r, z)$ to satisfy (2), where $B_r = \partial\psi/\partial r$, $B_\theta = ip\psi/r$, and $B_z = \partial\psi/\partial z$. Equation (3) gives the governing equation

$$\mathcal{H}_p(\psi) = 0 \tag{10}$$

in the insulator, where

$$\mathcal{H}_p = \frac{\partial^2}{\partial r^2} + \frac{1}{r}\frac{\partial}{\partial r} - \frac{p^2}{r^2} + \frac{\partial^2}{\partial z^2}. \tag{11}$$

With $\psi$ normalized by $\mu_0 J_o R$, (6) gives

$$\psi = -\frac{ia}{p}, \qquad \text{at } r = a. \tag{12}$$

As $(z/h) \to \infty$, the magnetic field perturbation created by the conductor decays exponentially, so that

$$\psi \to \Psi_o(r) = -\frac{ir^p}{pa^{p-1}}, \qquad \text{as } (z/h) \to \infty. \tag{13}$$

For the conductor, we eliminate $\boldsymbol{E}$ by substituting (5) into (1), and we normalize $\boldsymbol{B}$ and $\boldsymbol{j}$ with $\mu_0 J_o$ and $J_o/R$, respectively. Then (1)–(4) become

$$\frac{ip}{r} j_z - \frac{\partial j_\theta}{\partial z} = iR_\omega B_r \tag{14}$$

$$\frac{\partial j_r}{\partial z} - \frac{\partial j_z}{\partial r} = iR_\omega B_\theta \tag{15}$$

$$\frac{1}{r}\frac{\partial}{\partial r}(rj_\theta) - \frac{ip}{r} j_r = iR_\omega B_z \tag{16}$$

$$\frac{ip}{r} B_z - \frac{\partial B_\theta}{\partial z} = j_r \tag{17}$$

$$\frac{\partial B_r}{\partial z} - \frac{\partial B_z}{\partial r} = j_\theta \tag{18}$$

$$\frac{1}{r}\frac{\partial}{\partial r}(rB_\theta) - \frac{ip}{r} B_r = j_z \tag{19}$$

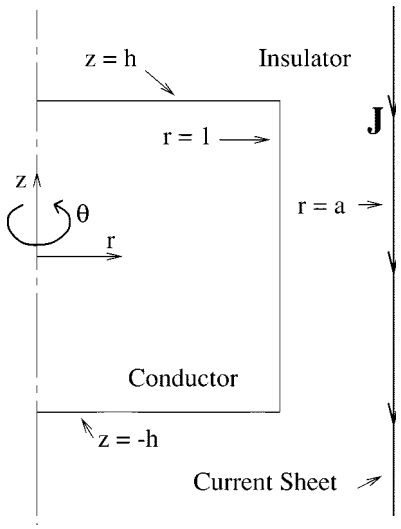


Fig. 1. Geometry with lengths normalized by the radius $R$ of the conducting cylinder. The axial electric current $\boldsymbol{J}$ concentrated at $r = a$ is periodic in both time and $\theta$.

$$\frac{1}{r}\frac{\partial}{\partial r}(rB_r) + \frac{ip}{r}B_\theta + \frac{\partial B_z}{\partial z} = 0 \tag{20}$$

$$\frac{1}{r}\frac{\partial}{\partial r}(rj_r) + \frac{ip}{r}j_\theta + \frac{\partial j_z}{\partial z} = 0 \tag{21}$$

where $R_\omega = \mu_0\sigma\omega R^2$ is the shielding parameter. We can discard (15) and (18) with no loss of determinacy.

We reduce the problem for the conductor to two scalar, complex functions, $Q_r(r, z) = rB_r$ and $B_z(r, z)$, and we obtain expressions for the other variables with the following steps. Equation (20) is an expression for $B_\theta$. Substituting this expression into (17) and (19) gives expressions for $j_r$ and $j_z$, so that (21) becomes an expression for $j_\theta$. Substituting these expressions into (14) and (16) gives the governing equations

$$\mathcal{H}_p(Q_r) + iR_\omega Q_r + 2\frac{\partial B_z}{\partial z} = 0 \tag{22}$$

$$\mathcal{H}_p(B_z) + iR_\omega B_z = 0. \tag{23}$$

For the elliptic operator $\mathcal{H}_p$, $r = 0$ is a regular singular point. The method of Frobenius [10] shows that the small-$r$ power series expansions for the two linearly independent solutions for $\psi$, $Q_r$, or $B_z$ have the form

$$r^s \sum_{n=0}^{\infty} f_n(z) r^{2n} \tag{24}$$

where $s = p$ or $s = -p$. The boundary conditions at $r = 0$ must exclude the solution with $s = -p$ for each variable.

## III. Hybrid Analytical Finite-Difference Solution

For the problem described in the previous section, we combine an analytical solution for $h \le z < \infty$ with finite-difference solutions for $0 \le z \le h$. This hybrid method has two advantages over a numerical treatment for the entire domain: 1) less memory is required because the total number of unknowns is much smaller and 2) there is no need to truncate the domain and to apply an artificial boundary condition at some large value of $z$.

There are now three domains in the $r - z$ plane, as sketched in Fig. 2: domain 1 is the conductor for $0 \le r \le 1$ and $0 \le z \le h$; domain 2 is the insulator between the conductor and the current sheet for $1 \le r \le a$ and $0 \le z \le h$; and domain 3 is the insulator above the conductor for $0 \le r \le a$ and $h \le z < \infty$. Equations (22) and (23) are the governing equations for domain 1, while (10) is the governing equation for both domains 2 and 3. The boundary conditions at $\Gamma_{1-2}$ between domains 1 and 2, and the boundary conditions at $\Gamma_{1-3}$ between domains 1 and 3 were presented in the previous section. The boundary at $\Gamma_{2-3}$ between domains 2 and 3 is an artifact of our hybrid method, so that $\psi$ should have a Taylor series in $(z - h)$ at each point along this boundary, and this series should be valid in both domains. Since (10) applies in both domains, continuity of $\psi$ and of $\partial\psi/\partial z$ at this boundary is sufficient to insure that all $z$ derivatives of $\psi$ are continuous here, so that such a Taylor series does exist.

For domain 3, the separation of variables solution that satisfies (10), (12), and (13), and which excludes $r^{-p}$ behavior near $r = 0$ is

$$\psi = \Psi_o(r) + \sum_{n=1}^{\infty} A_n J_p\left(\frac{\lambda_n r}{a}\right)\exp\left[-\frac{\lambda_n}{a}(z - h)\right] \tag{25}$$

where $J_p$ is the Bessel function of the first kind and of order $p$, while $\lambda_n$ are the roots of $J_p(\lambda_n) = 0$. The conditions at the boundary at $z = h$ with domains 1 and 2 determine the coefficients $A_n$.

For domain 2, we introduce $\psi = \Psi_o(r) + \Psi(r, z)$, where $\Psi$ also satisfies (10). The discrete algebraic equations for domains 1 or 2 were derived using a standard second-order finite-difference method with a regular grid. There are $(nr1 + 1 \times nz + 1)$ grid points for domain 1 and $(nr2 + 1 \times nz + 1)$ grid points for domain 2. The grid points in the $z$ direction for both domains are $z_j = (j-1)\Delta Z$, for $j = 1$ to $(nz+1)$, where $\Delta Z = h/nz$. The grid points in the $r$ direction for domain 1 are $r_i = (i-1)\Delta R1$, for $i = 1$ to $(nr1 + 1)$, where $\Delta R1 = 1/nr1$, and for domain 2 are $r_i = 1 + (i - 1)\Delta R2$, for $i = 1$ to $(nr2 + 1)$, where $\Delta R2 = (a - 1)/nr2$. To solve the set of discrete equations in either domain, we used the solver "hwscyl.f" in the FISHPACK library [11], which we modified for complex values.

### A. Boundary Conditions at $\Gamma_{1-2}$

The boundary conditions at $\Gamma_{1-2}$ involve matching two finite-difference solutions, which is currently being studied by many researchers as part of the domain decomposition used for parallel computing. The boundary condition on domain 2 at $\Gamma_{1-2}$ is the value of $\partial\Psi/\partial r$ computed from the solution in domain 1

$$\frac{\partial\Psi}{\partial r}(1, z_j) = Q_{r(nr1+1,\,j)} + ia^{(1-p)}, \quad \text{for } j = 1 \text{ to } (nz + 1). \tag{26}$$

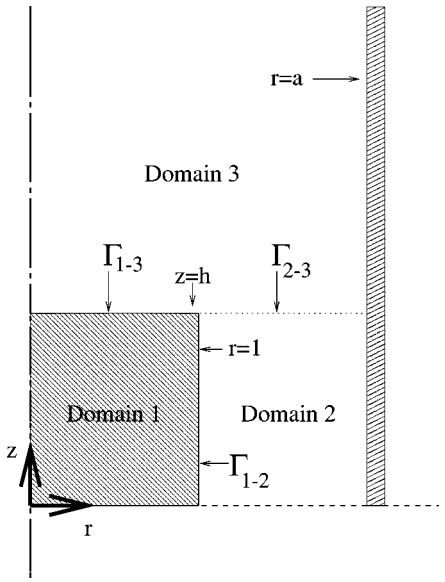


Fig. 2. Domains for the hybrid solution with boundaries $\Gamma_{1-2}$ at $r = 1$ for $0 \le z \le h$ between domains 1 and 2, $\Gamma_{1-3}$ at $z = h$ for $0 \le r \le 1$ between domains 1 and 3, and $\Gamma_{2-3}$ at $z = h$ for $1 \le r \le a$ between domains 2 and 3.

The boundary conditions on domain 1 at $\Gamma_{1-2}$ are the values of $\partial Q_r/\partial r$ and $B_z$ computed from the solution in domain 2. For $\partial Q_r/\partial r$, we use (10) evaluated at $r = 1$, so that

$$\frac{\partial Q_r}{\partial r}(1, z_j) + \frac{ip}{a^{(p-1)}} - p^2\Psi_{1,j} = \begin{cases} \dfrac{2}{(\Delta Z)^2}(\Psi_{1,1} - \Psi_{1,2}), \\ \quad \text{for } j = 1 \\ \dfrac{1}{(\Delta Z)^2}(2\Psi_{1,j} - \Psi_{1,j+1} - \Psi_{1,j-1}), \\ \quad \text{for } j = 2 \text{ to } nz \\ \dfrac{2}{(\Delta Z)^2}(\Psi_{1,nz+1} - \Psi_{1,nz} - (\Delta Z)B_z(1, h)), \\ \quad \text{for } j = (nz+1). \end{cases} \tag{27}$$

In order to obtain a second-order accurate expression for $B_z(1, h) = \partial\Psi/\partial z(1, h)$ from the solution for domain 2, we used the Taylor series expansion of $\Psi$ around $r = 1$ and $z = h$, and we used (10) evaluated at this point

$$B_z(1, h) = \frac{\Psi_{1,nz+1} - \Psi_{1,nz}}{\Delta Z} + \frac{\Delta Z}{2} \cdot \left\{ \left( \frac{2}{\Delta R2} - 1 \right) \left[ Q_{r(nr1+1,\,nz+1)} + ia^{(1-p)} \right] + p^2\Psi_{1,nz+1} - \frac{2}{(\Delta R2)^2} \cdot (\Psi_{2,nz+1} - \Psi_{1,nz+1}) \right\}. \tag{28}$$

The other values of $B_z$ are

$$B_z(1, z_j) = \begin{cases} 0, & \text{for } j = 1 \\ \dfrac{\Psi_{1,j+1} - \Psi_{1,j-1}}{2\Delta Z}, & \text{for } j = 2 \text{ to } nz. \end{cases} \tag{29}$$

### *B. Boundary Conditions at $\Gamma_{1-3}$ and $\Gamma_{2-3}$*

The coefficients $A_n$ in the solution (25) for domain 3 are determined from the values of $B_z(r, h)$ computed from the finite difference solutions in domains 1 and 2. Using the orthogonality of the Bessel functions

$$A_n = \frac{-2}{\lambda_n a[J_{(p-1)}(\lambda_n)]^2} \int_0^a rB_z(r, h)J_p\left(\frac{\lambda_n r}{a}\right) dr \tag{30}$$

for $n = 1$ to $nt$, where (25) is truncated after $n = nt$. The integral in (30) is evaluated using a linear interpolation between adjacent radial grid points

$$B_z(r, h) = B_z(r_i, h) + [B_z(r_{i+1}, h) - B_z(r_i, h)](r - r_i)/\Delta Rk \tag{31}$$

for $r_i \le r \le r_{i+1}$, where $k = 1$ or 2 for domain 1 or 2. Equation (28) gives $\partial\Psi/\partial z$ at $r = 1$ and $z = h$, while Taylor series in $(z - h)$ and (10) evaluated at $z = h$ were used to obtain second-order accurate expressions for the other values of $\partial\Psi/\partial z$ at $z = h$ from the solution for domain 2 in (32) at the bottom of the page.

The boundary condition for domain 2 at $\Gamma_{2-3}$ is the value of $\Psi$ computed from the solution (25) for domain 3

$$\Psi_{i,nz+1} = \sum_{n=1}^{nt} A_n J_p\left(\frac{\lambda_n r_i}{a}\right), \qquad \text{for } i = 1 \text{ to } (nr2+1). \tag{33}$$

The boundary conditions for domain 1 at $\Gamma_{1-3}$ are the values of $Q_r$ and $\partial B_z/\partial z$ computed from the solution (25) for domain 3

$$Q_{r(i,\,nz+1)} = -\frac{ir_i^p}{a^{(p-1)}} + \frac{r_i}{a}\sum_{n=1}^{nt} A_n\lambda_n J_p'\left(\frac{\lambda_n r_i}{a}\right) \tag{34}$$

$$\frac{\partial B_z}{\partial z}(r_i, h) = \frac{1}{a^2}\sum_{n=1}^{nt} \lambda_n^2 A_n J_p\left(\frac{\lambda_n r_i}{a}\right) \tag{35}$$

for $i = 1$ to $(nr1+1)$, where the prime denotes differentiation of the Bessel function.

For domain 1, we found that the boundary conditions

$$B_z = Q_r = 0, \qquad \text{at } r = 0 \tag{36}$$

excluded the $r^{-p}$ behavior and led to the small-$r$ behavior corresponding to (24) with $s = p$.

$$\frac{\partial\Psi}{\partial z}(r_i, h) = \frac{\Psi_{i,nz+1} - \Psi_{i,nz}}{\Delta Z} - \frac{\Delta Z}{2}\left\{ \frac{\Psi_{i+1,nz+1} - \Psi_{i-1,nz+1}}{2r_i(\Delta R2)} + \frac{\Psi_{i+1,nz+1} - 2\Psi_{i,nz+1} + \Psi_{i-1,nz+1}}{(\Delta R2)^2} - \frac{p^2\Psi_{i,nz+1}}{r_i^2} \right\}, \quad \text{for } i = 2 \text{ to } nr2 \tag{32}$$

Our iterative solution sequence involved the following steps:

1) use the modified "hwscyl.f" to solve for $Q_r$ and $B_z$ in domain 1 with the boundary conditions at $\Gamma_{1-2}$ from domain 2 and at $\Gamma_{1-3}$ from domain 3;
2) use the modified "hwscyl.f" to solve for $\Psi$ in domain 2 with the boundary conditions at $\Gamma_{1-2}$ from domain 1 and at $\Gamma_{2-3}$ from domain 3;
3) compute $A_n$ from (30)–(32).

A relaxation factor was included for each calculation of a new boundary condition for an adjacent domain.

## IV. Test Problem

In order to validate our hybrid analytical finite-difference method, we applied it to a mathematically similar problem which has a simple analytical solution. The real scalar function $T(x, y)$ in a plane with the Cartesian coordinates $x$ and $y$ has the same domains and boundaries as those in Fig. 2 with $r$ and $z$ replaced by $x$ and $y$, respectively. The governing equations are

$$\frac{\partial^2 T}{\partial x^2} + \frac{\partial^2 T}{\partial y^2} = RT \tag{37}$$

for domain 1, where $R$ is a parameter, and

$$\frac{\partial^2 T}{\partial x^2} + \frac{\partial^2 T}{\partial y^2} = 0 \tag{38}$$

for domains 2 and 3. The conditions are that $T$ and $\partial T/\partial x$ are continuous at $\Gamma_{1-2}$, $T$, and $\partial T/\partial y$ are continuous at both $\Gamma_{1-3}$ and $\Gamma_{2-3}$

$$T = 1, \qquad \text{at } x = a \tag{39}$$

$$T \to \left(\frac{x}{a}\right), \qquad \text{as } y \to \infty \tag{40}$$

while $T$ is an odd function of $x$ and an even function of $y$.

The analytical solutions are

$$T = \left(\frac{x}{a}\right) + \sum_{n=1}^{\infty} A_n \sin\left(\frac{n\pi x}{a}\right) \exp\left[-\left(\frac{n\pi}{a}\right)(y-h)\right] \tag{41}$$

for domain 3

$$T = \sum_{n=1}^{\infty} B_n \sin\left[\frac{n\pi(x-1)}{(a-1)}\right] \cosh\left[\frac{n\pi y}{(a-1)}\right] + \left(\frac{1-C_o}{a-1}\right) x + \left(\frac{aC_o - 1}{a-1}\right) + \sum_{n=1}^{\infty} C_n \sinh\left[\left(\frac{n\pi}{h}\right)(a-x)\right] \cos\left(\frac{n\pi y}{h}\right) \tag{42}$$

for domain 2, and

$$T = \sum_{n=1}^{\infty} D_n \sin(n\pi x) \cosh(\alpha_n y) + \sum_{n=0}^{\infty} E_n \sinh(\beta_n x) \cos\left(\frac{n\pi y}{h}\right) \tag{43}$$

for domain 1, where $\alpha_n = (R + n^2\pi^2)^{1/2}$ and $\beta_n = [R + (n\pi/h)^2]^{1/2}$. Using the orthogonality of the trigonometric functions: 1) continuity of $\partial T/\partial y$ at $\Gamma_{1-3}$ or $\Gamma_{2-3}$ gives an explicit expression for each $D_n$ or each $B_n$ as a sum over the $A_n$'s; 2) continuity of $T$ and $\partial T/\partial x$ at $\Gamma_{1-2}$ gives explicit expressions for each $C_n$ and each $E_n$ in terms of $B_n$ and $D_n$, and hence in terms of the $A_n$'s; and 3) substitution of these expressions into the continuity of $T$ at $\Gamma_{1-3}$ and $\Gamma_{2-3}$ gives a set of simultaneous linear algebraic equations for the $A_n$'s.

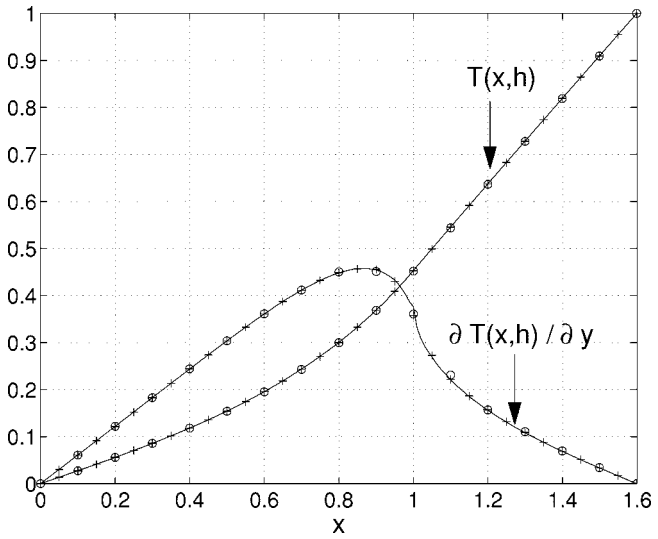


Fig. 3. The values of $T$ and $\partial T/\partial y$ at $y = h$ from the analytical solution, from the hybrid method with the coarse grid, and from the hybrid method with the fine grid are denoted by the continuous lines, the open circles, and the crosses, respectively.

We combine the analytical solution (41) for domain 3 with the finite-difference solutions of (37) for domain 1 and of (38) for domain 2. At $\Gamma_{1-2}$, continuity of $T$ or $\partial T/\partial x$ is the boundary condition on domain 2 or 1, respectively. The values of $\partial T/\partial y$ from the solution (41) for domain 3 are the boundary conditions at $\Gamma_{1-3}$ and $\Gamma_{2-3}$ on domains 1 and 2. The values of $T$ at $y = h$ from domains 1 and 2 are used to compute the $A_n$ in (41) with a linear interpolation for $T$ between $x$ grid points to evaluate the integral of $\sin(n\pi x/a)T(x, h)$ from $x = 0$ to $x = a$.

We present test-problem results for $R = 10$, $h = 3$, and $a = 1.599$, where this peculiar value of $a$ was chosen to avoid the special treatment of terms in the analytical solution with integer values of $n/a$ or $n/(a-1)$. For the domains 1 and 2 finite-difference solutions, we used both a coarse grid, with $nx1 = 10$, $nx2 = 6$, and $ny = 30$, and a fine grid with $nx1 = 20$, $nx2 = 12$, and $ny = 60$. Matching the finite-difference and analytical solutions at $y = h$ is the critical step in the hybrid method, so we first compare results along this line. The values of $T$ and $\partial T/\partial y$ at $y = h$ from the analytical solution and from the hybrid method with both grids are plotted in Fig. 3. Even the coarse grid gives good results, while the fine grid gives even better results.

The accuracy of the hybrid method for this test problem is further illustrated by comparing the values of the coefficients $A_n$ in the domain 3 solution (41) from the entirely analytical method and from the hybrid analytical–numerical method. The first five coefficients from the analytical solution and the absolute value of the difference between each value and the corresponding value from the hybrid solution with the coarse or fine grid are presented in Table I. With an even finer grid, $|An_{num} - An_{anal}|$

is comparable to $10^{-5}$, which is the order of the error in our entirely analytical solution due to the truncation of the set of simultaneous, linear, algebraic equations for the coefficients $A_n$. In the hybrid solution, a relaxation factor of 0.5 was used in the calculation of revised boundary conditions for an adjacent domain. Forty iterations of the sequential solution for the three domains was sufficient to achieve convergence for all grids considered.

## V. Magnetic Field Results

Having validated the hybrid analytical finite-difference method for the mathematically similar test problem described in Section IV, we now apply this method to the problem described in Sections II and III for a rotating magnetic field with a conducting cylinder. We present results for $p = 1$, $a = 1.6$, and for three combinations of values for $R_\omega$ and $h$, each chosen to provide a further validation of the hybrid method.

### A. Results for $R_\omega = 100$ and $h = 0.8$

In the asymptotic solution for $R_\omega \gg 1$, the magnetic field in the conducting cylinder is confined to skin-depth layers that are adjacent to the boundaries $\Gamma_{1-2}$ at $r = 1$ and $\Gamma_{1-3}$ at $z = h$, and which have an $O(R_\omega^{-1/2})$ dimensionless thickness. In the numerical solution for relatively large values of $R_\omega$, it is important to resolve these layers. We found that values of $\Delta R1$ and $\Delta Z$ equal to approximately $0.2R_\omega^{-1/2}$ provided excellent resolution, and we generally chose $\Delta R2$ to be close to $\Delta R1$. For $R_\omega = 100$ and $h = 0.8$, a grid with $nr1 = 45$, $nr2 = 27$ and $nz = 36$ and $nt = 144$ gave excellent results, while further grid refinement for domains 1 and 2 led to very small changes in the results. We found that 0.45 was the optimum relaxation factor in the revision of the boundary conditions for the adjacent domains, and that 50 iterations were sufficient to achieve convergence.

In order to validate the hybrid analytical finite-difference solution for this case, we also obtained a solution using finite differences everywhere. For this fully numerical solution, domain 3 was truncated at $z = 3h = 2.4$ and $\Psi$ was set equal to zero here. The differences between the results of the fully numerical and hybrid solutions are extremely small everywhere in all three domains.

Since the critical steps in the hybrid approach are the matchings at $r = 1$ and $z = h$, we first look at the values of $B_r$ and $B_z$ along these matching lines and continuing along $r = 1$ into domain 3 to $z = 1.5$. The plots of the real and imaginary parts of $B_r$ and $B_z$ along these lines are presented in Fig. 4. The most likely site for a problem in the hybrid approach is the junction of the three domains at $r = 1$ and $z = h$. The results in Fig. 4 clearly demonstrate that this point is not a problem for the hybrid approach. This success of the hybrid approach is further demonstrated by the excellent agreement with the all finite-difference solution, where the domain matchings use standard and well-validated finite-difference methods.

In Section II, the solution of Maxwell's equations in the conducting cylinder was reduced to two scalar equations (22) and (23) governing $Q_r = rB_r$ and $B_z$. The values of $B_\theta$ and $\boldsymbol{j}$ in the conductor are determined as part of the post processing after the iterative, sequential solution for the three domains converges. In Section II, we indicated that $B_\theta$ can be determined from (20) once $Q_r$ and $B_z$ are known. This method works well for small values of $R_\omega$ and for most of the domain 1 for large values of $R_\omega$, but (20) gives erroneous results for $B_\theta$ near $r = 1$ and $z = h$ for even moderately large values of $R_\omega$. In the asymptotic solution for $R_\omega \gg 1$, the two skin-depth layers intersect to form a corner region with $\Delta r = O(R_\omega^{-1/2})$ and $\Delta z = O(R_\omega^{-1/2})$ adjacent to the corner at $r = 1$ and $z = h$. Inside this corner region, the leading-order terms in (20) are $\partial Q_r/\partial R + \partial B_z/\partial Z$, where $R$ and $Z$ are the appropriately stretched local radial and axial coordinates, while $B_\theta$ only enters (20) for this corner region for the higher order perturbations of $Q_r$ and $B_z$. The numerical solution for $R_\omega = 100$ has exactly the behavior expected from the large-$R_\omega$ corner region. Near $r = 1$ and $z = h$, $\partial Q_r/\partial r$ and $\partial B_z/\partial z$ both become very large, have very nearly equal magnitudes, and have opposite signs. Therefore, computing $B_\theta$ from (20) involves the difference between two nearly equal values, thus losing all accuracy locally. A mathematically equivalent and numerically accurate method to determine $B_\theta$ during postprocessing is to solve an elliptic equation governing $Q_\theta = rB_\theta$, which is obtained by substituting (17), (19), and (20) into (15)

$$\mathcal{H}_p(Q_\theta) - \frac{2}{r}\frac{\partial Q_\theta}{\partial r} + iR_\omega Q_\theta = -\frac{2ip}{r^2}Q_r. \tag{44}$$

For the large-$R_\omega$ analysis, (44) leads directly to the correct equations governing the $O(1)B_\theta$ in the corner region and in both skin-depth layers, so that (44) is a uniformly valid equation for $B_\theta$ over the entire domain 1 for all values of $R_\omega$, including $R_\omega \gg 1$. The boundary conditions are

$$Q_\theta = ip\psi, \qquad \text{at } r = 1 \tag{45}$$

$$Q_\theta = ip\psi, \qquad \text{at } z = h \tag{46}$$

$$Q_\theta = 0, \qquad \text{at } r = 0 \tag{47}$$

TABLE I
First Five Coefficients in the Domain 3 Part of the Entirely Analytical Solution and the Magnitude of the Difference Between Each Coefficient and the Corresponding Coefficient in the Hybrid Solution with Both Grids

| $n$ | $An_{anal}$ | $\lvert An_{num} - An_{anal}\rvert$ *coarse grid* | $\lvert An_{num} - An_{anal}\rvert$ *fine grid* |
|---|---|---|---|
| 1 | $-1.8656e-01$ | $0.91e-3$ | $0.22e-3$ |
| 2 | $-8.4544e-03$ | $0.46e-3$ | $0.10e-3$ |
| 3 | $+1.1563e-02$ | $0.15e-3$ | $0.03e-3$ |
| 4 | $-1.4927e-03$ | $0.09e-3$ | $0.02e-3$ |
| 5 | $-2.1908e-03$ | $0.18e-3$ | $0.03e-3$ |

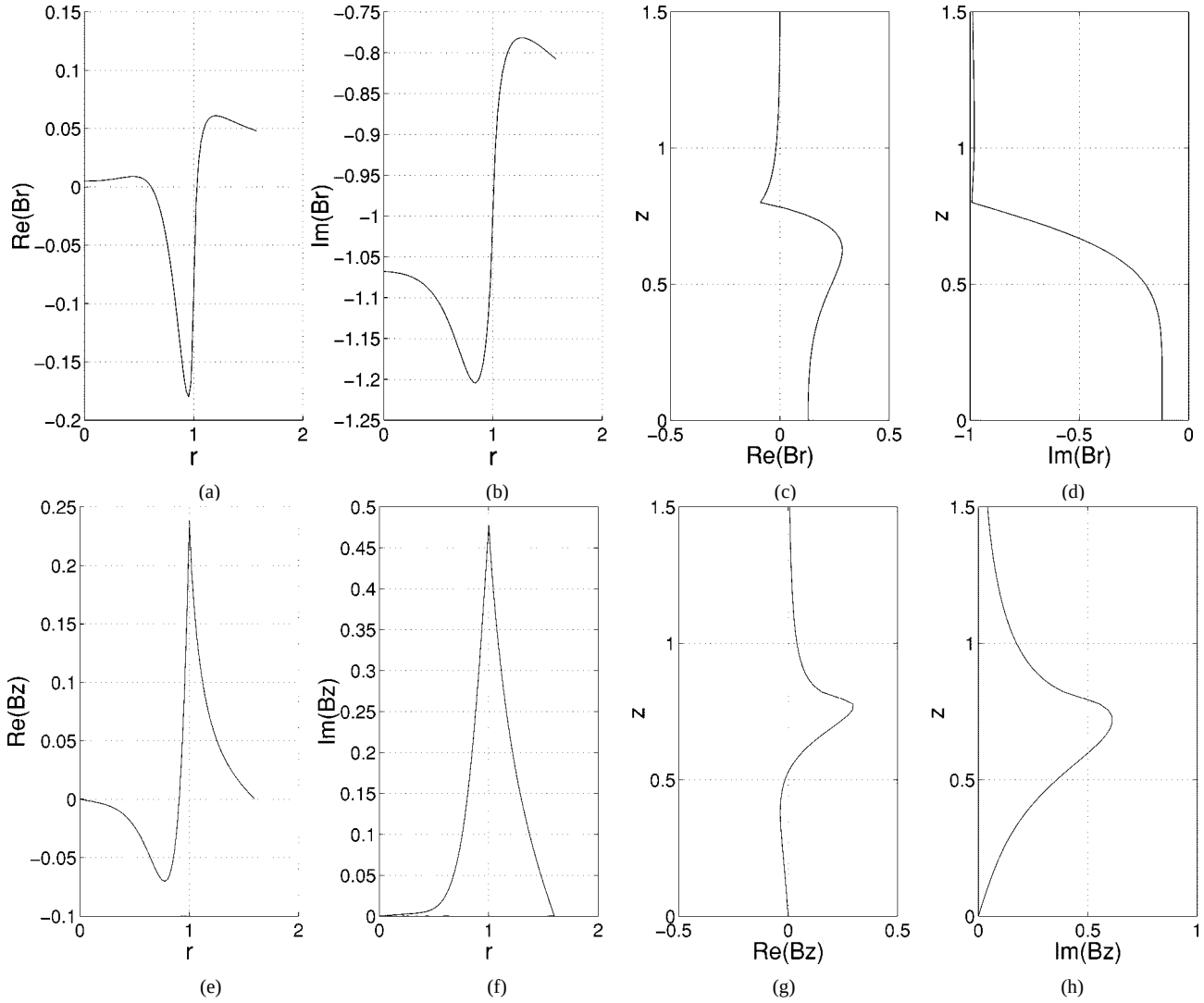


Fig. 4. $B_r$ and $B_z$ at $r = 1$ and $z = h$ for $R_\omega = 100, h = 0.8$ and $a = 1.6$. (a) $\Re e(B_r)$ at $z = h$. (b) $\Im m(B_r)$ at $z = h$. (c) $\Re e(B_r)$ at $r = 1$. (d) $\Im m(B_r)$ at $r = 1$. (e) $\Re e(B_z)$ at $z = h$. (f) $\Im m(B_z)$ at $z = h$. (g) $\Re e(B_z)$ at $r = 1$. (h) $\Im m(B_z)$ at $r = 1$.

where the values of $\psi$ in (45) and (46) are computed from the finite-difference solution for domain 2 and from the analytical solution for domain 3, respectively. In addition, $Q_\theta$ is an even function of $z$. Contours of the real and imaginary parts of $B_\theta$ are presented in Fig. 5. The skin-depth layers and the corner region formed by the intersection of the skin-depth layers are evident in both parts of Fig. 5, although they are not very thin for $R_\omega = 100$. Clearly $\Delta R1 = \Delta Z = 0.2R_\omega^{-1/2} = 0.02$ is more than adequate to resolve the gradients near $r = 1$ and $z = h$.

### B. Results for $R_\omega = 100$ and $h = 3.0$

For this case, we used grids for domains 1 and 2 with $nr1 = 45$, $nr2 = 27$, and $nz = 135$ and we used $nt = 144$. In both the conductor and the insulator, the results for $0 \le z \le 1$ are virtually independent of $z$. Therefore, we expect the results at $z = 0$ for $h = 3.0$ to match the results for an infinitely long cylinder. For $h = \infty$, all variables are independent of $z$, $B_z = 0$, $B_r = ipA/r$, and $B_\theta = -dA/dr$, where $A(r)$ is the complex modal function for the $z$ component of the magnetic vector potential. There is a simple analytical solution [7] for the coupled ordinary differential equations governing $A(r)$, namely $A = (2a/D_p)J_p(\alpha r)$ for $0 \le r \le 1$, and

$$A = \frac{a}{pD_p}\left[\{2pJ_p(\alpha) - \alpha J_{p+1}(\alpha)\}r^p + \alpha J_{p+1}(\alpha)r^{-p}\right] \tag{48}$$

for $1 \le r \le a$, where $\alpha = (iR_\omega)^{1/2}$ and $D_p = \alpha(a^p + a^{-p})J_{p+1}(\alpha) - 2a^p p J_p(\alpha)$. The real and imaginary parts of $B_r$ and $B_\theta$ for $R_\omega = 100$ and $a = 1.6$ from the solution for the infinitely long cylinder and from the hybrid solution for $h = 3$, evaluated at $z = 0$, are plotted in Fig. 6. The agreement is excellent.

### C. Results for $R_\omega = 1000$ and $h = 0.8$

The results presented in Fig. 5 for $R_\omega = 100$ have the qualitative features of the asymptotic solution for $R_\omega \gg 1$, but the regions of nonzero magnetic field are not thin, so that we would not expect good quantitative agreement.

In order to approach quantitative agreement with the large-$R_\omega$ solution, we applied the hybrid method to the case with $R_\omega = 1000$ and $h = 0.8$. For the grids in domains 1 and

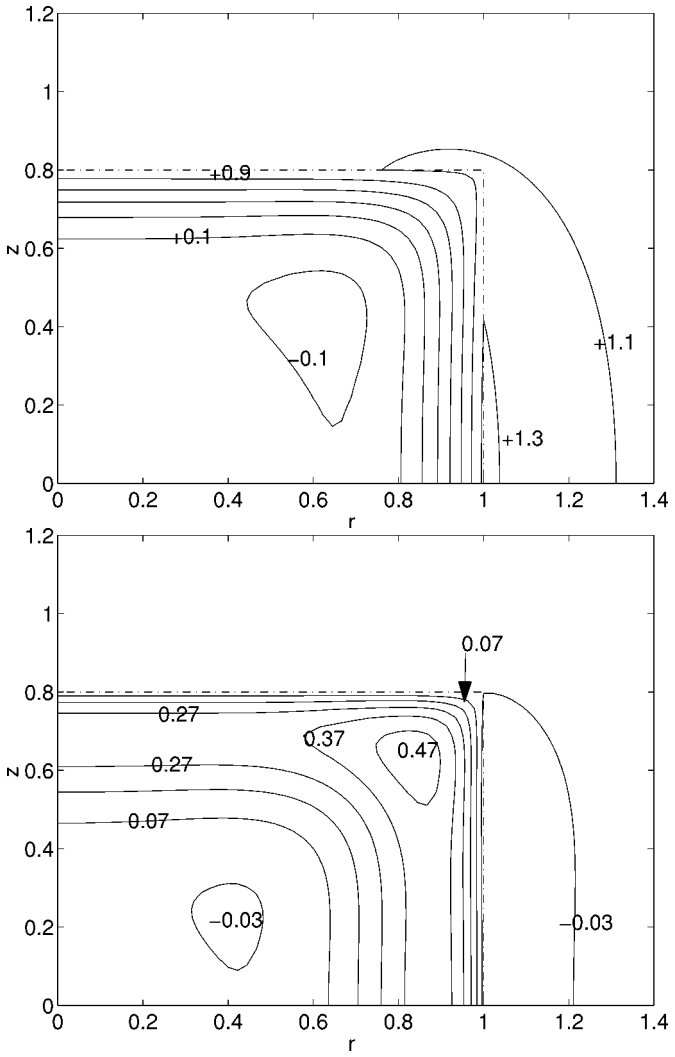


Fig. 5. Contours of the real and imaginary parts of $B_\theta$ for $R_\omega = 100, h = 0.8$ and $a = 1.6$. (a) $\Re e(B_\theta) = -0.1 + 0.2k$ for $k = 0$ to 7. (b) $\Im m(B_\theta) = -0.03 + 0.1k$ for $k = 0$ to 5. The dash-dot lines represent the cylinder's borders.

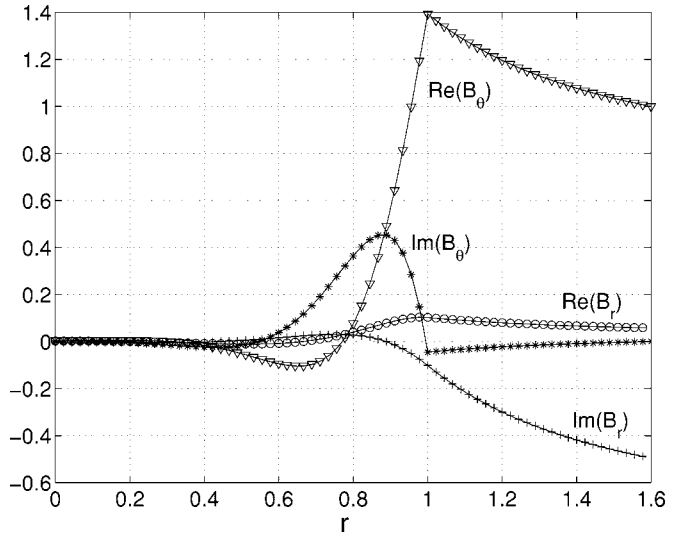


Fig. 6. Real and imaginary parts of $B_r$ and $B_\theta$ for $R_\omega = 100$ and $a = 1.6$. Values from the analytical solution for an infinitely long conducting cylinder are denoted by the continuous lines, while values at $z = 0$ from the hybrid solution for $h = 3$ are denoted by various symbols.

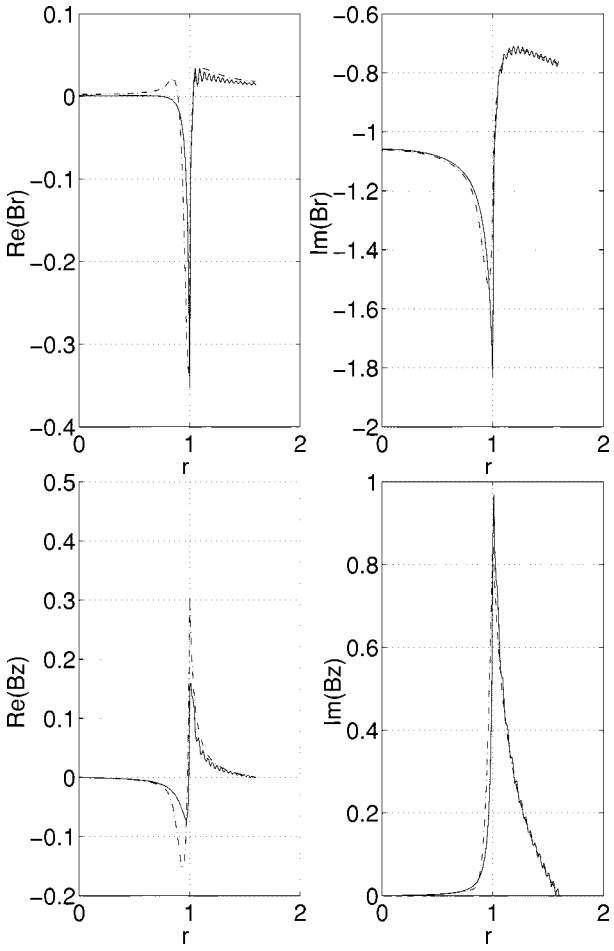


Fig. 7. Real and imaginary parts of $B_r$ and $B_z$ at $z = h$ for $R_\omega = 1000$ and $h = 0.8$. The dot-dash lines are the results of the hybrid solution for arbitrary $R_\omega$ and the solid lines are the results of the approximate solution for $R_\omega \gg 1$.

2, $nr1 = 150$, $nr2 = 90$, and $nz = 120$, for the truncated series in domain 3, $nt = 480$, and for the boundary conditions between domains the relaxation factor equals 0.45. Again, roughly 50 iterations were sufficient to achieve convergence.

Equations (17)–(20) with $j_r = j_\theta = j_z = 0$ govern $B_r$, $B_\theta$, and $B_z$ in domains 2 and 3. Since these equations do not involve $R_\omega$, the perturbations for $R_\omega \gg 1$ in domains 2 and 3 arise from the matching conditions at $r = 1$ and $z = h$. The derivation of the asymptotic solution for $R_\omega \gg 1$ in the conducting cylinder follows a standard procedure and leads to successive boundary conditions on the various orders of $B_r$ at $r = 1$ and of $B_z$ at $z = h$. We derived approximate solutions for domains 2 and 3 by combining the $O(1)$ and $O(R_\omega^{-1/2})$ boundary conditions at each boundary. This approximate solution neglects $O(R_\omega^{-1})$ terms. The boundary conditions on the approximate solutions for domains 2 and 3 are given by the solutions in the skin-depth layers in the conducting cylinder

$$B_r + \frac{(1+i)}{(2R_\omega)^{1/2}}\left[iB_\theta + \frac{\partial B_z}{\partial z}\right] = 0 \tag{49}$$

for domain 2 at $r = 1$ for $0 \le z \le h$, and

$$B_z + \frac{(1+i)}{(2R_\omega)^{1/2} r}\left[\frac{\partial}{\partial r}(rB_r) + iB_\theta\right] = 0 \tag{50}$$

for domain 3 at $z = h$ for $0 \leq r \leq 1$. Since $R_\omega$ appears in (49) and (50), a value of $R_\omega$ must be specified, but the asymptotic solution for domains 2 and 3 also assumes that $R_\omega$ is sufficiently large that $O(R_\omega^{-1})$ terms are negligible. The analytical solution (25) was used for domain 3, and a numerical solution was used for domain 2. In addition to the boundary conditions (49) and (50), the approximate solutions for domains 2 and 3 are matched at the boundary $\Gamma_{2-3}$ at $z = h$ for $1 \leq r \leq a$.

The values of $B_r$ and $B_z$ at $z = h$ from the hybrid solution and from the large-$R_\omega$ approximate solution for $R_\omega = 1000$ and $h = 0.8$ are plotted in Fig. 7. The oscillations in the approximate results arise from a Gibbs phenomenon because the series (25) must match a discontinuity in slope at $r = 1$. This discontinuity does not exist in reality or in the arbitrary-$R_\omega$ hybrid solution, but it enters the large-$R_\omega$ approximate solution because the latter neglects the smoothing due to the $O(R_\omega^{-1/2}) \times O(R_\omega^{-1/2})$ corner region in the conductor, since this smoothing is formally $O(R_\omega^{-1})$. The agreement in Fig. 7 is generally very good, and, where there are differences, the hybrid solution is probably more accurate because the corner region is clearly still playing an important role for $R_\omega = 1000$. An extension to a approximate, large-$R_\omega$ solution including $O(R_\omega^{-1})$ terms would involve solving an elliptic problem for the corner region, which is comparable to the elliptic problem for domain 1 in the hybrid solution. Therefore, the hybrid solution with adequate resolution near $r = 1$ and $z = h$ probably gives better results than any practical asymptotic solution, even for very large values of $R_\omega$. Meyer *et al.* [6] reached the same conclusion for the induction heating and magnetic levitation with purely azimuthal electric currents.

## VI. Concluding Remarks

This paper focuses on a rotating magnetic field in an infinite domain with a finite-dimension electrical conductor surrounded by an electrical insulator. The equations for the insulator often lead to simple analytical solutions. For the present geometry, the insulator solution involves separation of variables, while other geometries might lead to the superposition of Green's functions or to a Fourier transform solution. The hybrid approach combines the simple analytical solution for the infinite region of the insulator with numerical solutions for the finite-dimension conductor and for a small adjacent insulator region. The key step in this hybrid approach is the accurate matching between the analytical and numerical solutions at the interfaces of their domains. The advantages of this hybrid approach over a purely numerical solution are: 1) there are fewer unknowns and 2) there is no need for artificial conditions at boundaries where the infinite domain is truncated. On the other hand, the computer time required to accurately evaluate the Bessel-function integrals in (30) partially offsets the reduction in computer time gained with fewer unknowns.

Here we treated a problem which is periodic in time. Since (2) and (3) with $\boldsymbol{j} = 0$ for the insulator do not involve a time derivative, the hybrid approach can be applied to much more general transient problems in which the insulator solution is an instantaneous solution which matches and provides boundary conditions for the transient problem in the electrical conductor. Therefore, numerical time integration is only required for the conductor with time-independent boundary conditions at each interface with the insulator. This approach has been previously applied to dynamo problems with an electrically conducting sphere surrounded by an unbounded insulator [12]. The separation-of-variables solution for the insulator then involves various spherical harmonic functions. Thus, we have applied a method previously used for dynamo problems to the geometry of crystal-growth processes with RMF's from finite-radius inductors. Our solution applies when the axial length of the inductor is longer than the axial length of the liquid region.

## References


[1] P. A. Davidson and J. C. R. Hunt, "Swirling recirculating flow in a liquid-metal column generated by a rotating magnetic field," *J. Fluid Mech.*, vol. 185, pp. 67–106, 1987.

[2] Y. M. Gelfgat, L. A. Gorbunov, and V. Kolevzon, "Liquid metal flow in a finite-length cylinder with a rotating magnetic field," *Exp. Fluids*, vol. 15, pp. 411–416, 1993.

[3] Y. M. Gelfgat and J. Priede, "MHD flows in a rotating magnetic field (a review)," *Magnetohydrodyn.*, vol. 31, no. 1/2, pp. 188–200, 1995.

[4] R. F. Dudley and P. E. Burke, "The prediction of current distribution in induction heating installations," *IEEE Trans. Ind. Applicat.*, vol. IA-8, pp. 565–571, 1972.

[5] J. D. Lavers and P. P. Biringer, "The influence of system geometry on the electromagnetic stirring forces in crucible induction melting furnaces," in *Metallurgical Applications of Magnetohydrodynamics*, H. K. Moffatt and M. R. E. Proctor, Eds. London, U.K.: Metals Soc., 1982, pp. 62–78.

[6] J. L. Meyer, J. Szekely, N. El-Kaddah, C. Vivès, and R. Ricou, "Electromagnetic and fluid flow phenomena in a mercury model system of the electromagnetic casting of aluminum," *Met. Trans. B*, vol. 18 B, pp. 539–548, 1987.

[7] L. Martin Witkowski and P. Marty, "Effect of a rotating magnetic field of arbitrary frequency on a liquid metal colum," *Eur. J. Mech. B/Fluids*, vol. 17, no. 2, pp. 239–254, 1998.

[8] K. Mazuruk, N. Ramachandran, M. P. Volz, and D. Gillies, "Study of frequency effects of a rotating magnetic field on fluid flow in vertical cylinders," in *Materials Research in Low Gravity*, N. Ramachandran, Ed. San Diego, CA: Soc. Photo-optical Instrum. Eng., 1997, vol. 3123, pp. 262–270.

[9] P. A. Davidson, "Swirling flow in an axisymmetric cavity of arbitrary profile, driven by a rotating magnetic field," *J. Fluid Mech.*, vol. 245, pp. 669–699, 1992.

[10] F. B. Hildebrand, *Advanced Calculus for Applications*. Englewood Cliffs, NJ: Prentice-Hall, 1976.

[11] R. Sweet, "A cyclic reduction algorithm for solving block tridiagonal systems of arbitrary dimensions," *SIAM J. Numer. Anal.*, vol. 14, pp. 706–720, 1977.

[12] D. R. Fearn, P. H. Roberts, and A. M. Soward, "Convection, stability and the dynamo," in *Energy Stability and Convection*, G. P. Galdi and B. Straughan, Eds. Harlow, U.K.: Longman Scientific, 1988, pp. 60–324.